sustainability

MDPI

Article

Early Identification and Influencing Factors Analysis of Active Landslides in Mountainous Areas of Southwest China Using SBAS−InSAR

Peilian Ran [1], Shaoda Li [1,*], Guanchen Zhuo [1], Xiao Wang [2], Mingjie Meng [3], Liang Liu [1], Youdong Chen [1], Huina Huang [4], Yu Ye [5] and Xiangqi Lei [1]

[1] College of Earth Science, Chengdu University of Technology, Chengdu 610059, China
[2] School of Architecture and Civil Engineering, Chengdu University, Chengdu 610106, China
[3] Sichuan Institute of Land and Space Ecological Restoration and Geological Hazard Prevention, Chengdu 610081, China
[4] Disaster Reduction Center of Fujian, Fuzhou 350013, China
[5] Chengdu Qingbaijiang District Land Reserve Center, Chengdu 610399, China
* Correspondence: lisd@cdut.edu.cn

Abstract: Potential landslides in the mountainous areas of southwest China pose a serious threat to the lives and property of local residents. Synthetic aperture radar interferometry (InSAR) technology has the advantages of wide coverage, all weather applicability, and low cost and can quickly and accurately identify large range of active landslides, making it a useful geodetic tool for the early identification and prevention of landslides. This paper employed small baseline subset InSAR (SBAS−InSAR) technology and ascending and descending Sentinel−1 data from January 2019 to December 2021 to early identify active landslides in the Maoxian County to Li County National Highway (G317 and G213). The InSAR deformation results were verified by geometric distortion analysis, optical remote sensing interpretation, and field investigation, and 115 active landslides were successfully determined, among which 23 active landslides were identified by ascending and descending Sentinel−1 data together. In addition, InSAR deformation results show that fault, stratigraphic lithology, and rainfall are the three main factors that accelerate the deformation of active landslides and can trigger new active landslides. This study can provide an important reference for the early identification and prevention of landslides in mountainous areas.

Keywords: SBAS−InSAR; Sentinel−1; southwest China; landslide identification; visibility; influencing factors

Citation: Ran, P.; Li, S.; Zhuo, G.; Wang, X.; Meng, M.; Liu, L.; Chen, Y.; Huang, H.; Ye, Y.; Lei, X. Early Identification and Influencing Factors Analysis of Active Landslides in Mountainous Areas of Southwest China Using SBAS−InSAR. *Sustainability* **2023**, *15*, 4366. https://doi.org/10.3390/su15054366

Academic Editors: Wen Nie and Haijun Qiu

Received: 29 December 2022
Revised: 13 February 2023
Accepted: 20 February 2023
Published: 1 March 2023

1. Introduction

As one of the most dangerous geohazards, landslide hazards are widely distributed in the world. The mountainous areas of southwest China are located in the eastern part of the Qinghai–Tibet Plateau, where the terrain is undulating and the geological environment is complex, breeding a large number of landslide hazards [1–5]. Therefore, early identification of active landslides in the mountainous areas of southwest China is of great significance for geohazards prevention. However, due to the complex terrain conditions in the mountainous areas of southwest China, traditional geological survey methods are difficult to carry out efficiently and widely. With the continuous development of earth observation technology, SBAS−InSAR technology can fully and effectively use long-span radar images to continuously monitor surface deformation [6–9]. It effectively solves the problem that spatiotemporal incoherence and atmospheric effects affect the monitoring accuracy [10,11]. Because of its advantages of high monitoring accuracy, wide monitoring range, and all weather applicability, it has been widely used in the early identification and monitoring of landslide hazards. For example, Dai et al. [12] used SBAS−InSAR technology

to identify 23 active landslides in the surrounding areas of Zhouqu County, Gansu Province. Dun et al. [13] used SBAS−InSAR technology to identify 25 active landslides in Baihetan Reservoir in Jinsha River Basin. Liu et al. [14] used InSAR technology to identify more than 900 active landslides in the Jinsha River basin. However, due to the complex geomorphology and geological conditions in the mountainous areas, the early identification of landslides using InSAR is still challenging and is limited by many factors, such as serious geometric distortions which exist in the mountainous areas [15–17]. Therefore, it is necessary to analyze the spatial distribution of geometric distortions and the influence on the early identification results, verifying the accuracy of the early identification results using InSAR. In addition, it is also of great significance to know about the influencing factors of active landslides for the purpose of prevention of landslides in mountainous areas.

In this paper, firstly, SBAS−InSAR technology was used to obtain the deformation information of a large range in the study area by combining the ascending and descending Sentinel−1 data. Secondly, the InSAR deformation results were verified by geometric distortion analysis, optical remote sensing interpretation, and field investigation to determine the active landslide. Finally, the influencing factors of landslides were analyzed with respect to faults, stratigraphic lithology, and rainfall in detail.

2. Study Area

The study area in this paper is along the National Highway (G213 and G317) from Mao County to Li County, Sichuan Province, which spans Mao County, Wenchuan County, and Li County, with a total area of about 864 km^2. The study area is located in the eastern Qinghai–Tibet Plateau region of the upper reaches of Minjiang river, on the landscape which belongs to the mountains and steep terrain slopes. The relative elevation difference is big, with an altitude of 474–6250 m, an average elevation of 3362 m. The gully aspect has the typical geomorphic features of alpine valleys (Figure 1b), with regional faults (fold and fault are a sign of tectonic activity) [18]. There are four main fault zones, namely, the Xiongershan fault zone and Pingtoushan fault zone in Li County, and the steep-up fault zone and Maowen fault zone in Wenchuan County and Mao County (Figure 2). The stratigraphic development in Figure 2 includes Proterozoic (Middle Proterozoic monzogranite, grey-greenish-fuchsia basic-medium acid volcanic rocks, clastic rocks, carbonate rocks), Permian system (lower volcanic lava, pyroclastic rock, upper tuffaceous sandstone, carbonate rock, bottom shale, siltstone), Devonian system (lower clastic rock, upper carbonate rock, greyish white limestone, bioclastic limestone, intercloud limestone, algal limestone, greyish black metamorphic mud, sand, carbonaceous rock, inter-carbonate rock), Sinian system (metamorphic sandstone, mellite, crystalline limestone, dolomite, lower sandstone, shale, conglomerate, sandy shale, dolomite), Triassic system (metamorphic sandstone, SLATE, limestone, dark gray thin-thick metamorphic feldspar quartz sandstone, pebbled sandstone and carbonaceous SLATE interbedded), Carboniferous (limestone mixed mudstone, argillaceous limestone), and Silurian (green sericeous SLATE, sandy limestone, quartz sandstone).

The study area has a plateau monsoon climate, with a great difference in altitude and complex topography and a remarkable vertical zonal climate, which has the characteristics of mountainous vertical-type climates. The annual temperature range is small, and the daily temperature range is large. The annual average temperature is 11.3 °C, with a range of 10~12 °C. Affected by the topography, the spatial distribution of rainfall is extremely uneven, with less in the middle and gradually increasing to the periphery. In terms of seasonal distribution, the precipitation in winter and spring is less than that in winter, often with dry winter and spring drought, while the precipitation in summer and autumn is more than that in April to October, accounting for more than 90% of the annual precipitation [14,19]. The increase of rainfall will lead to frequent occurrence of landslide hazards. For example, the 2008 Wenchuan earthquake induced the Daguangbao huge landslide [20]. The area of landslides and collapses induced by the Lushan earthquake in 2013 was about 1300 km^2 [21]. In 2013, a heavy rainstorm broke out in Wenchuan County, resulting in mass

debris flow along national Highway 213 and provincial highway 210, etc. [22]. Landslides occurred in Xishan Village of Li County [23] in 2016 and Xinmo Village of Mao County [24] in 2017, which caused serious loss of life and property.

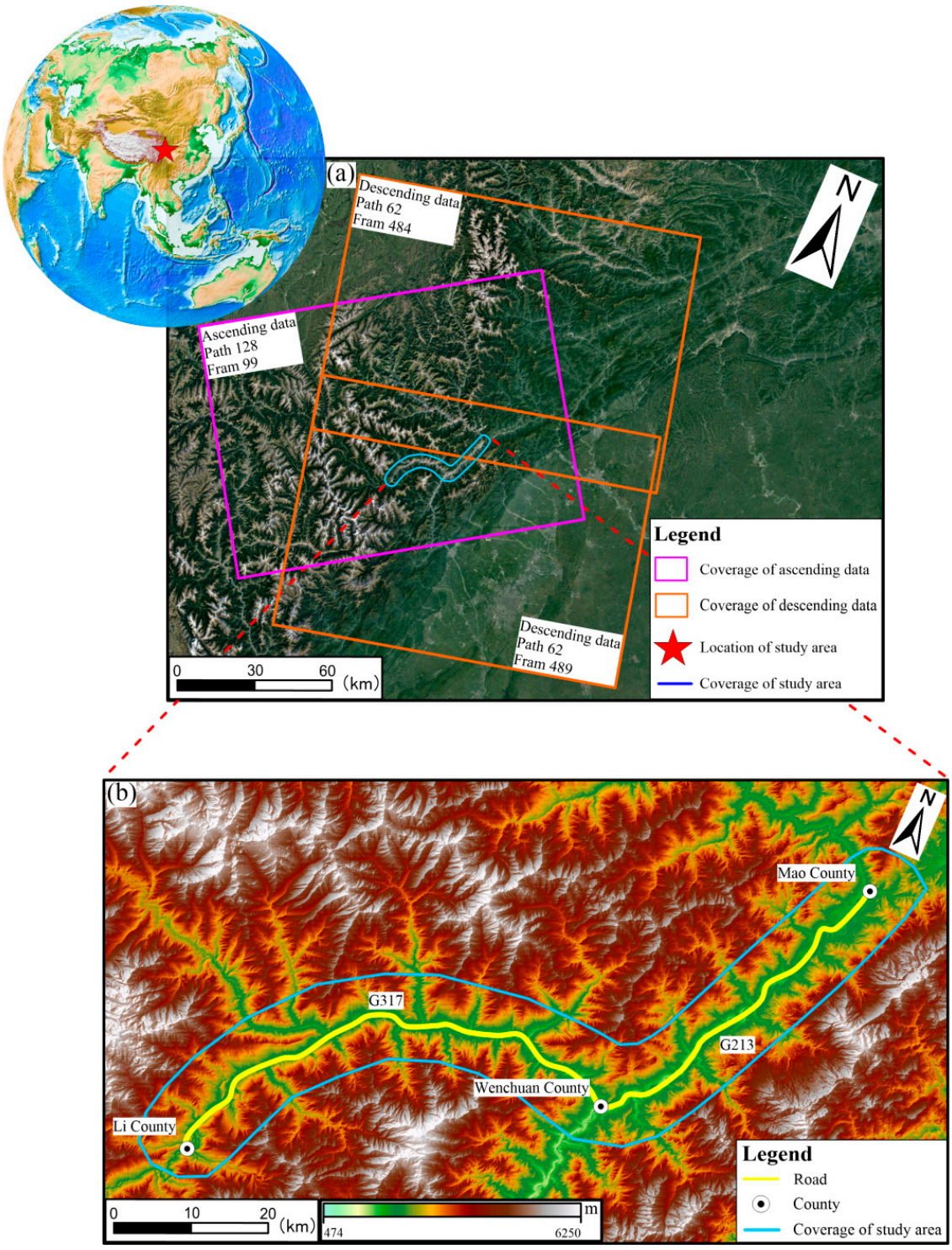

Figure 1. SAR data coverage in the study area. (**a**) Coverage of ascending and descending Sentinel−1 images and (**b**) elevation of the study area.

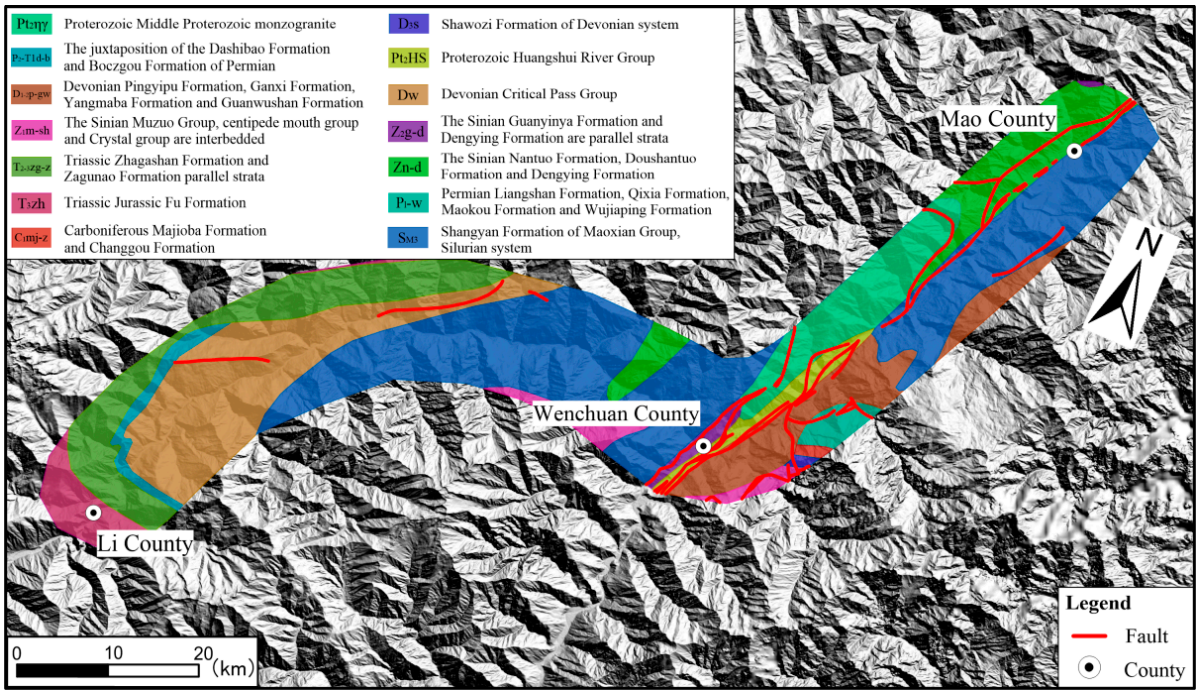

Figure 2. Regional geological map of the study area.

3. Data and Methodology

3.1. Data

Sentinel−1 is an Earth observation satellite launched by the European Space Agency (ESA) in 2014. It uses a binary orbiting mode and carries C-band synthetic aperture radar (SAR). It provides continuous satellite imagery with a short revisit period (12 days) and a large single image coverage area (250 × 250 km^2). In this study, 90 scene interferometric wide swath (IW) images of ascending covering the study area from 9 January 2019 to 24 December 2021 were used, and 81 scene interferometric wide swath (IW) images of descending covering the same area from 4 January 2019 to 13 December 2021 were used. The coverage area and frame of the image are shown in Figure 1a. The basic parameters of Sentinel−1 are shown in Table 1.

Table 1. Basic parameters of Sentinel−1 data in the study area.

Wavelength	Ascending/ Descending Track	Time	Return to the Cycle	Resolution	Angle of Incidence	Imaging Mode	Polarization Mode	Number of Image (Scene)
5.6 cm/C Band	Ascending track	9 January 2019~ 24 December 2021	12 Days	20 m	41.7°	IW	VV	90
5.6 cm/C Band	Descending track	4 January 2019~ 13 December 2021	12 Days	20 m	41.5°	IW	VV	81

In this study, the ALOS World 3D (AW3D30) digital surface model (DSM) provided by Japan Space Agency was used as the external digital elevation model (DEM) to remove the topographic effect. In addition, the Sentinel−1 precise orbit ephemerides (POD) data are used to correct the orbit errors, which means the systematic errors are effectively removed.

In the process of processing the data, the ENVI@SARscape software was used for data processing. The image of 10 March 2019 was used as the super main image for the ascending data, the image of 28 May 2019 was used as the super main image for the descending data, and the remaining image was used as the auxiliary image for registration with the super main image. The time baselines of ascending data and descending data are controlled within 60 days, and the space baselines are controlled within 180 m and 120 m, respectively.

A total of 427 interference pairs were generated by free combination of ascending data and 324 interference pairs were generated by free combination of descending data. The spatiotemporal baseline connection diagram of the ascending and descending data is shown in Figure 3.

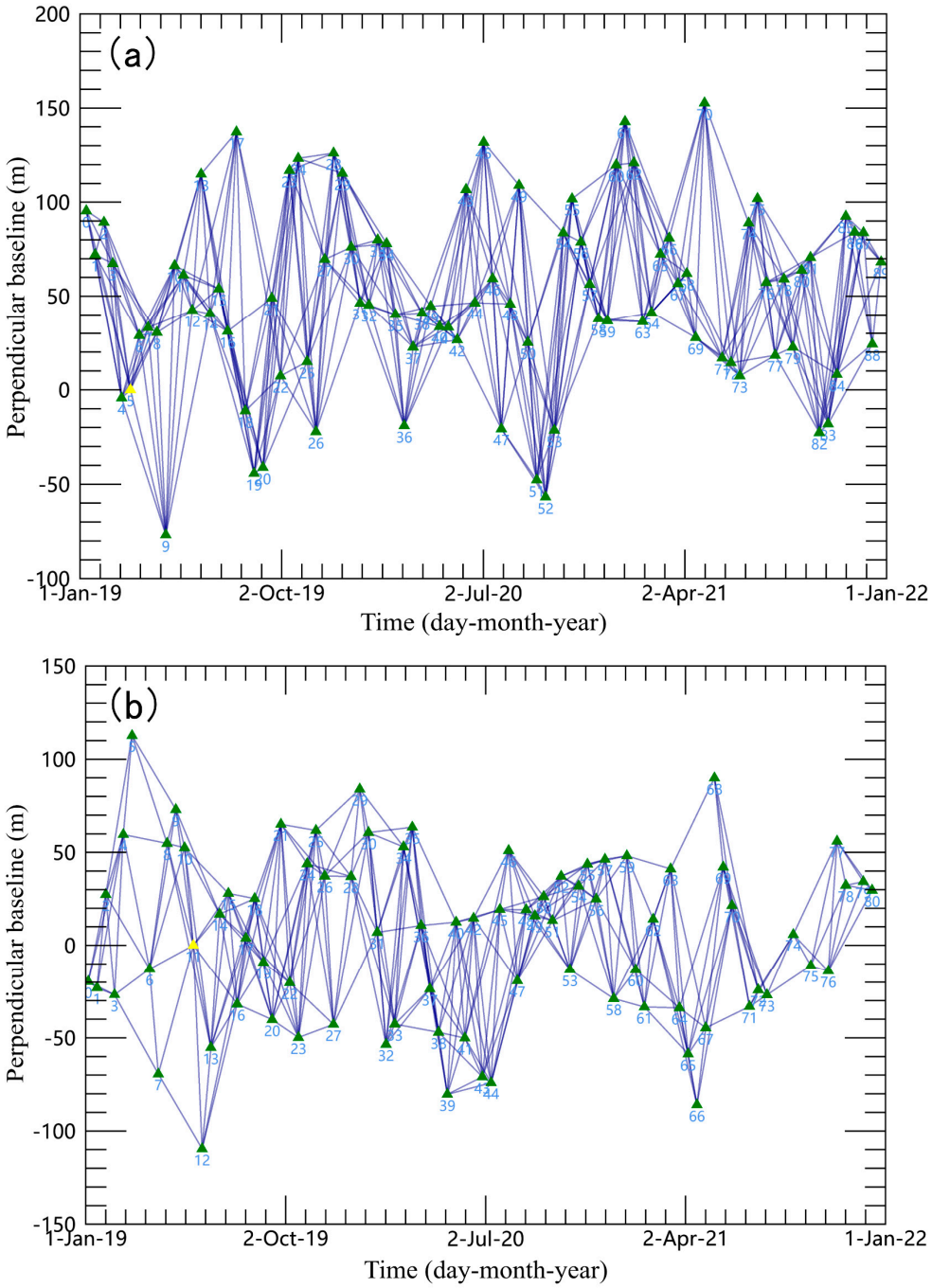

Figure 3. Time–position map of Sentinel−1 (**a**) ascending and (**b**) descending.

3.2. Methodology

SBAS−InSAR technology is a classical time series analysis method proposed by Berardino and Lanari et al., which is used for short baseline combination and large-scale deformation inversion [25]. According to the principle of short spatiotemporal baseline, the interferogram of time series of multi-main images is generated under the threshold limit of spatiotemporal baseline, and the singular value decomposition (SVD) method is used

to retrieve the deformation sequence and the average deformation rate of the study area during the observation time [26].

Assuming that the same area is covered in time series ($t_0, \ldots, t_N$) $N + 1$ SAR images, one of which is selected as the primary image for registration, appropriate time baseline and spatial baseline thresholds are set, and the remaining SAR images are registered with the primary image. A maximum of M differential interferograms can be generated from $N + 1$ SAR images, which meet the following expressions [25,27,28]:

$$\frac{N+1}{2} \leq M \leq N\left(\frac{N+1}{2}\right) \tag{1}$$

Minimum cost flow (MCF) method is used for phase unwrapping the interferogram. Assume that the j differential interferogram is generated from the SAR images acquired by the auxiliary image t_A and the primary image t_B at their respective time points, the pixel components in the interference phase can be expressed as follows:

$$\begin{aligned} \delta\varphi_j &= \varphi(t_B, x, r) - \varphi(t_A, x, r) \\ &\approx \tfrac{4\pi}{\lambda}[d(t_B, x, r) - d(t_A, x, r)] + \Delta\varphi^j_{topo}(x, r) \\ &+\Delta\varphi^j_{APS}(t_B, t_A, x, r) + \Delta\varphi^j_{noise}(x, r) \end{aligned} \tag{2}$$

where λ represents the wavelength of the imaging radar system, $d(t_B, x, r)$ and $d(t_A, x, r)$ are the cumulative deformation variables of the line of sight (LOS) direction of radar at t_B and t_A; $\Delta\varphi_{j,topo}(x, r)$ represents the residual terrain phase, which can be removed by external reference DEM; $\Delta\varphi_{j,APS}(t_B, t_A, x, r)$ is the atmospheric phase, which can be removed by high-pass filtering in space and low-pass filtering in time; $\Delta\varphi_{j,noise}(x, r)$ is the noise phase, which can be effectively removed by multi-looking and filtering [29].

After phase unwrapping is completed, a new linear equation will be established between linear deformation and DEM error phase; that is, residual elevation and deformation rate will be estimated based on the linear model, and the phases that are not unwrapped will be unwrapped twice. The expression is as follows:

$$[B, C]p' = \delta\varphi \tag{3}$$

where B is the matrix of $M \times N$, and C is the coefficient matrix related to the spatial baseline. The value of p' must satisfy the following relation:

$$p' = [v \ \ \Delta Z]^T \tag{4}$$

where v is the phase value matrix of the average deformation rate.

The detailed data processing process is as follows: first, linear deformation phase and DEM errors, including spatiotemporal incoherence, nonlinear deformation phase, and atmospheric delay phase, are removed in the process of generating differential interferograms to generate residual phase; second, the atmospheric delay phase and nonlinear deformation phase are separated by high-pass filtering in space and low-pass filtering in time; then, the least square method (LSM) and singular value decomposition (SVD) are used to solve the deformation of all interference pairs so as to obtain the deformation results of the time series; finally, the cumulative deformation variables and deformation rate in the SAR coordinate system are converted to the geographic coordinate system. The SBAS−InSAR technical process is shown in Figure 4.

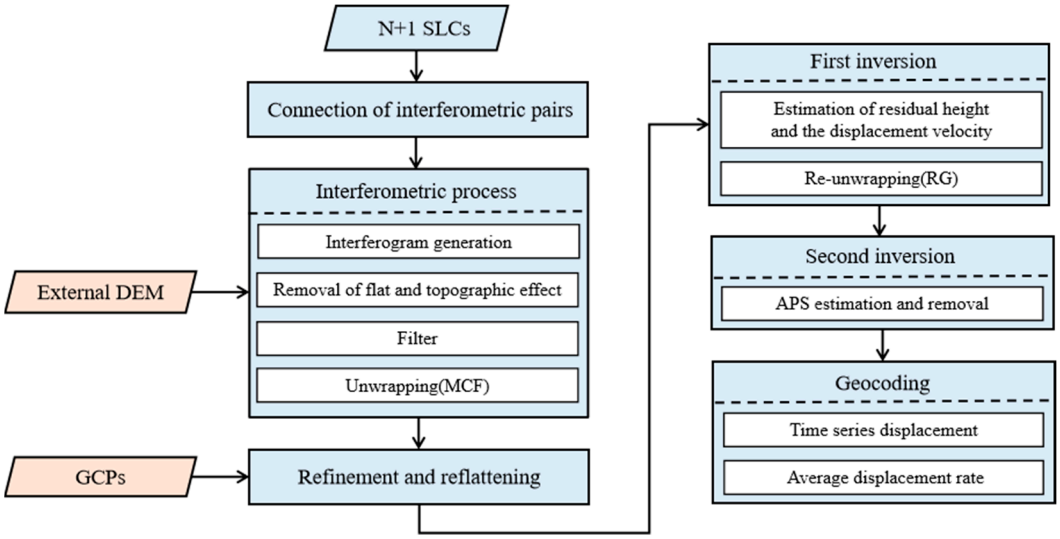

Figure 4. SBAS−InSAR technology flow chart.

4. Results and Analysis

4.1. Deformation Detection Results

When the geometric distortion generated by ascending and descending Sentinel−1 data in the study area is eliminated, the InSAR results obtained from ascending and descending Sentinel−1 data from January 2019 to December 2021 based on SBAS−InSAR technology do not show invalid deformation areas, and finally the deformation results along the LOS direction of the effective area from Mao County to Li County National Road (G317 and G213) are obtained, as shown in Figures 5 and 6.

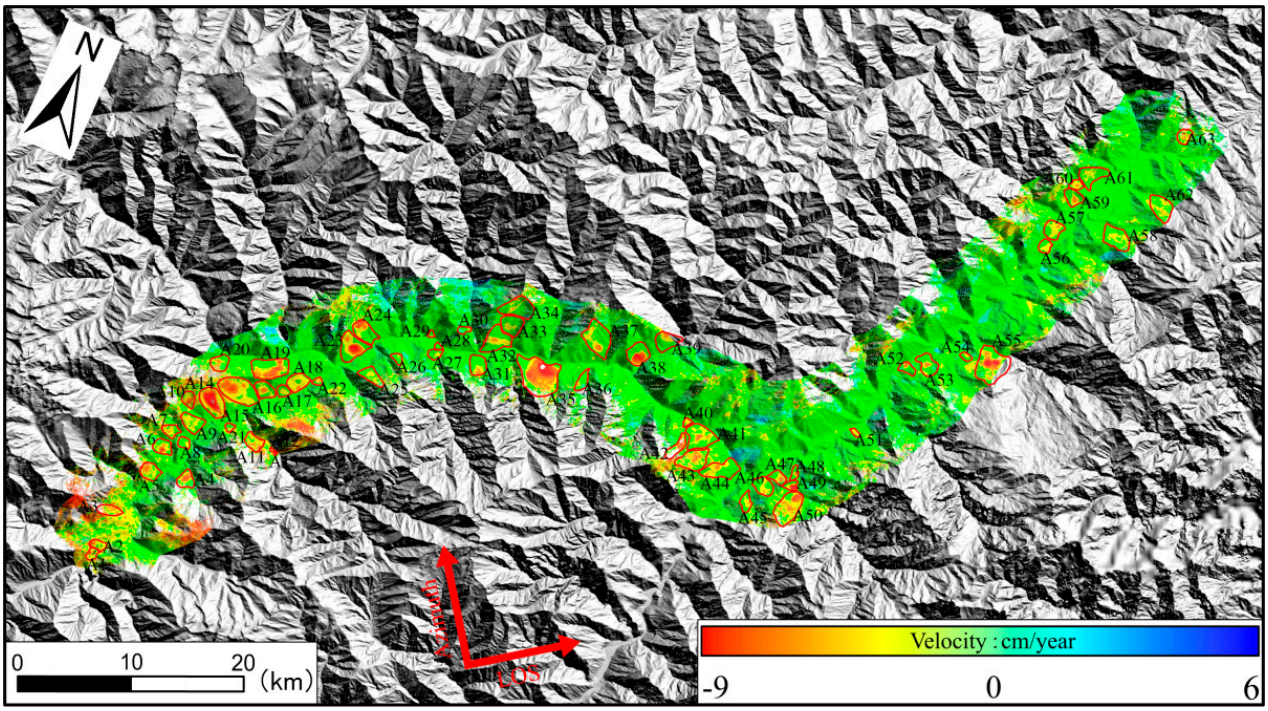

Figure 5. Deformation results of Sentinel−1 ascending data in the study area.

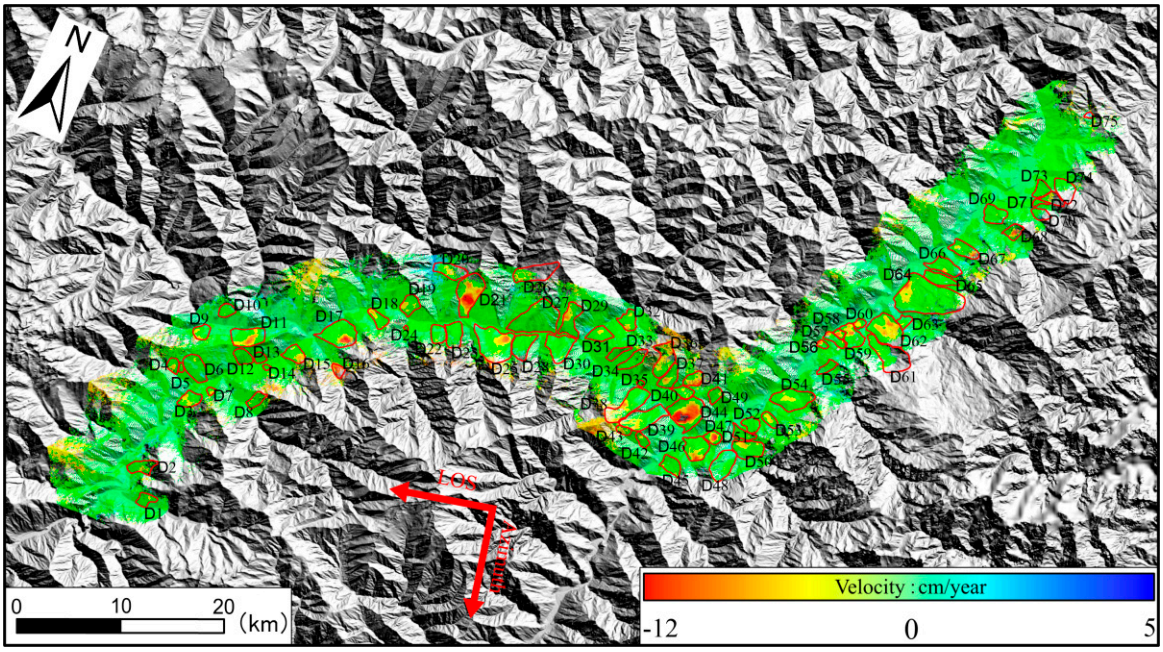

Figure 6. Deformation results of Sentinel−1 descending data in the study area.

The ascending Sentinel−1 data identified 12 more active landslides than the descending Sentinel−1 data. The ascending Sentinel−1 data identified 63 active landslides, A1−A63 in Figure 5. The descending Sentinel−1 data identified 75 active landslides, namely D1–D75 in Figure 6. Comparing the results of the ascending and descending, we found that the ascending and descending Sentinel−1 data identified 23 identical active landslides. It is mainly distributed in Ganbao Township (A10/D4, A14/D6, A21/D7), Xiameng Township (A20/D9, A19/D11), Xuecheng Town (A16/D12, A17/D13, A22/D15, A25/D17), Tonghua Township (A33 and A34/D21, A31/D22), and Taoping Town (A35/D25, A37/D27) in Li County; Weizhou Town (A41 and A42/D38, A43/D39, A46/D46, A47/D47, A50/D48, A51/D54) in Wenchuan County; Nanxin Town (A52/D57, A53/D59, A54/D62) and Fengyi Town (A62/D74) in Mao County. The deformation of landslide A14/D6, A19/D11, A25/D17, A33 and A34/D21, A35/D25, A50/D48, A52/D57, A53/D59, A54/D62 is more significant.

4.2. Mapping Active Landslides

The distribution maps of active landslides along Mao County to Li County National Road (G317 and G213) were drawn by using deformation rate map, topographic map, and Google Earth optical remote sensing image. The potential active landslides were determined using shape, size, and magnitude of deformation from the deformation measurement results, especially −10 cm/year for an active landslide. During this process, the deformation measurement results were used for location the active landslides, the Google Earth optical images were utilized for determining the active landslides boundaries [14], and the field investigation was applied for verifying the identified results. The ascending and descending Sentinel−1 data identified 115 active landslides, shown in dark blue in Figure 7. In order to show the deformation results of active landslides more clearly, 20 active landslides are highlighted (10 active landslides in ascending data and 10 active landslides in descending data), together with the deformation rate map and Google Earth optical remote sensing image map. It can be seen from Figure 8 that the deformation boundary obtained by SBAS−InSAR technology is in good agreement with the landslide boundary of Google earth optical remote sensing image. For landslide hazard, the region with the largest deformation rate has the strongest activity. The above research results show that SBAS−InSAR technology plays an important role in accurately delineating landslide

boundaries and identifying active landslides. Some active landslides found in this study are highly consistent with published literature [30,31], such as landslide A4−A6, A11, A14−A15, A18−A19, A22−A24, A32, A35, A37−A38, A40−A41, A44, A47−A50, A57, and A63 in Figure 5, and landslide D18–D19, D21, D25, D37, D40, D48, and D50 in Figure 6.

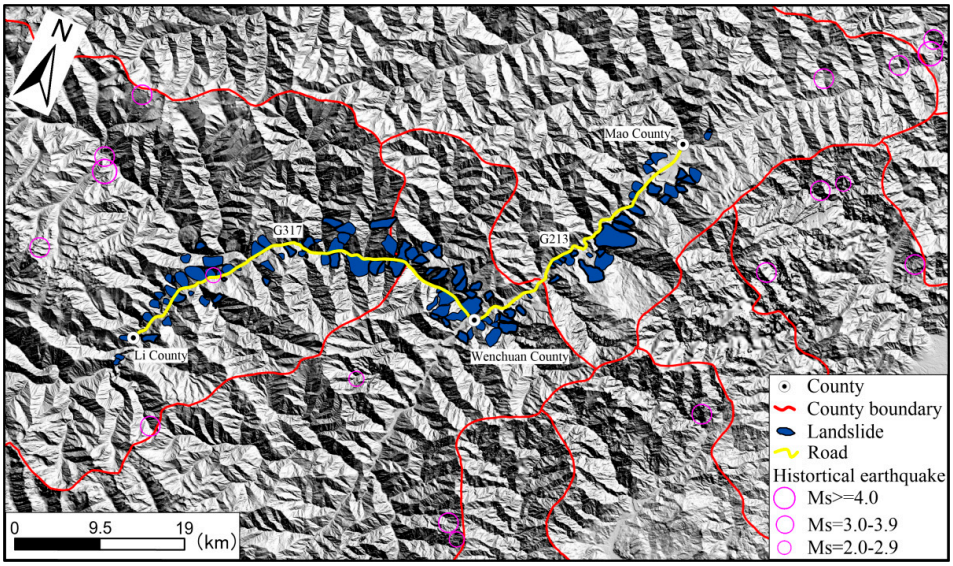

Figure 7. Distribution of active landslides detected by the Sentinel−1 images in the study area.

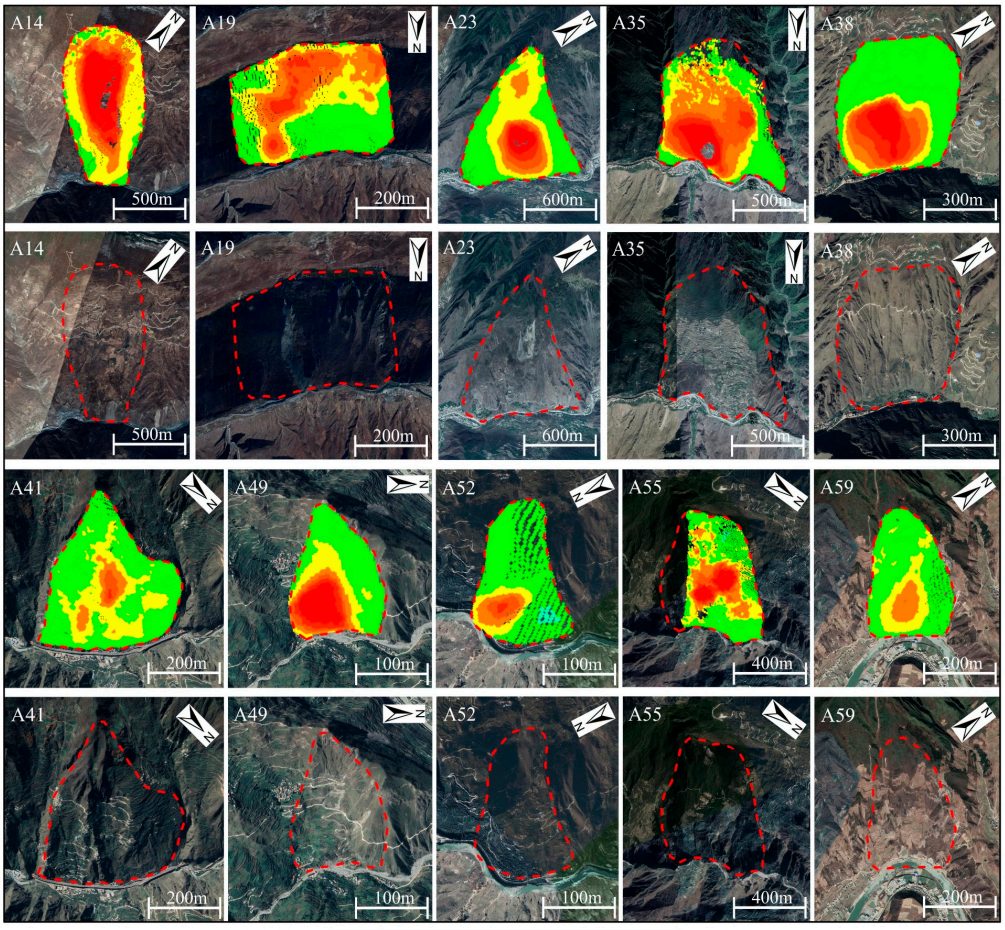

Figure 8. *Cont.*

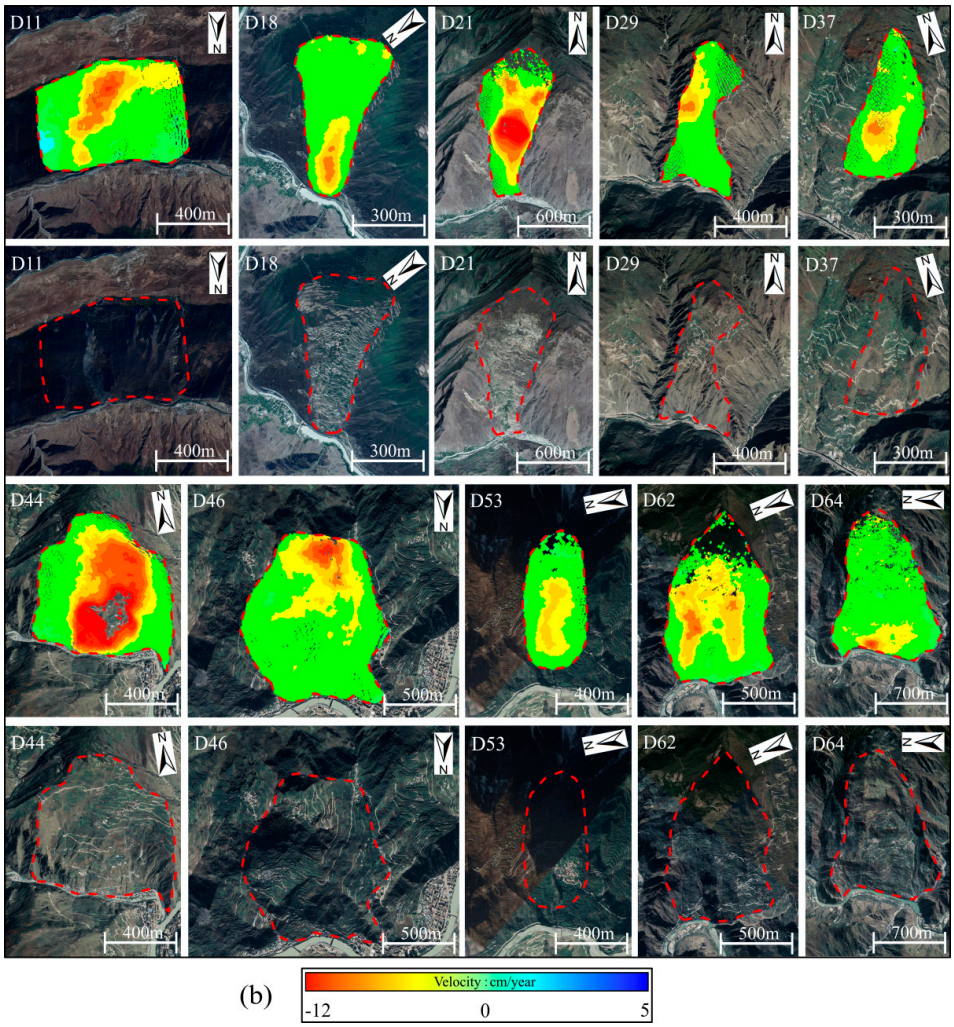

Figure 8. (**a**) Sentinel−1 ascending data enlarged deformation rate maps and optical remote sensing images of 10 exemplary landslides; (**b**) Sentinel−1 descending data enlarged deformation rate maps and optical remote sensing images of 10 exemplary landslides. The red solid lines indicate the boundaries of the landslides. The optical remote sensing images were sourced from the Google Earth platform.

5. Discussion

5.1. Impact Factors on the Results of Landslide Mapping

As the study area is located in the mountainous areas of southwest China, the terrain is steep, so there are inevitably geometric distortions in the study area [32]. Because of the difference of slope and aspect along the National Road (G317 and G213) from Mao County to Li County and the difference of the orbit flight Angle of Sentinel−1, the distribution of geometric distortion has regional differences. The research results of this paper show that the deformation results vary with different orbits (Figures 5 and 6). In order to quantitatively evaluate the geometric distortion distribution and characteristics of the ascending and descending Sentinel−1 data, the geometric distortion distribution and suitability of the study area can be accurately calculated based on the original image data and imaging parameters, as shown in Figures 9 and 10.

It can be seen from Figure 9 that the geometric distortion (layover and shadow) area of the ascending data in the study area is 204.77 km^2, accounting for 23.70% of the study area. It can be seen from Figure 10 that the geometric distortion (layover and shadow) area of the descending data is 220.15 km^2, accounting for 25.48% of the study area. This indicates

that SBAS−InSAR technology is not completely effective in monitoring this area; that is, there is a blind area for InSAR monitoring.

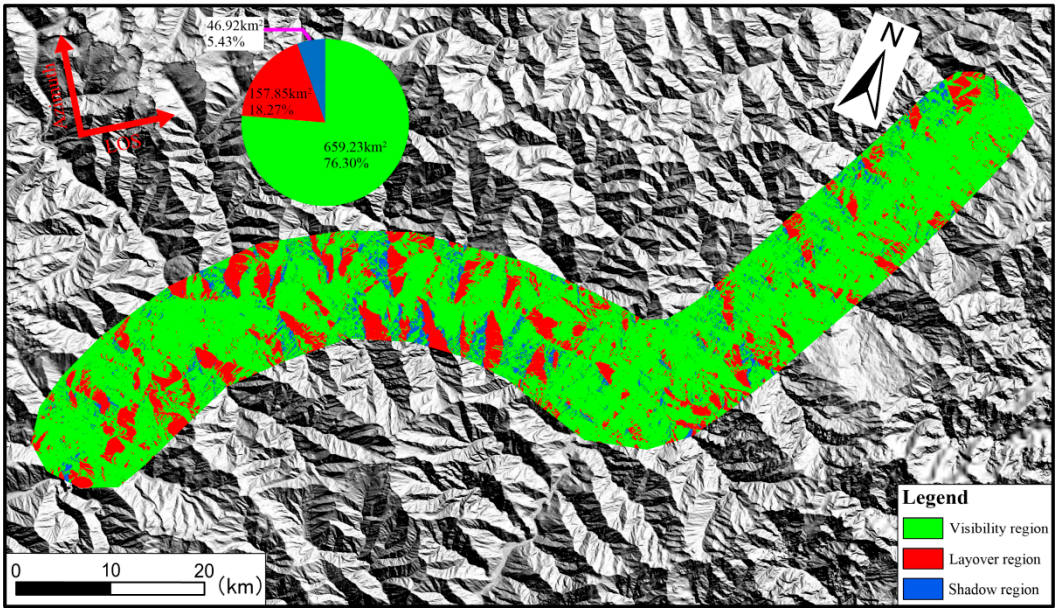

Figure 9. Geometrical distortions (layover and shadow) and visibility of the ascending Sentinel−1 images in the study area.

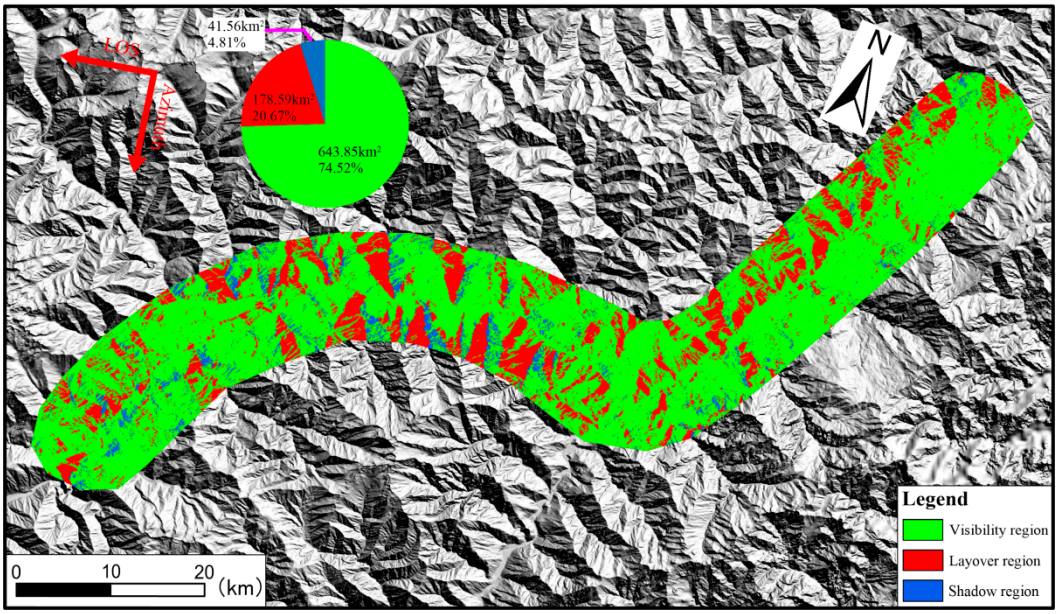

Figure 10. Geometrical distortions (layover and shadow) and visibility of the descending Sentinel−1 images in the study area.

It can be seen from Figures 9 and 10 that it is difficult for single orbit data to comprehensively obtain deformation information in the study area. The effective observation area of ascending Sentinel−1 data accounts for 76.30% of the total area, while the effective observation area of descending Sentinel−1 data accounts for 74.52% of the total area. However, the joint monitoring of ascending and descending Sentinel−1 data increased the effective observation area to 89.14% (Figure 11) and improved the monitoring coverage of deformation information in the study area. Therefore, in order to prevent the reduction of the effective observation area caused by topographic factors, the method of combining the ascending and descending Sentinel−1 data is adopted to effectively reduce the

defects that cannot be effectively observed due to geometric distortion so as to improve the effective utilization of satellite data. In addition, in the deformation calculation of some areas, the combination of ascending and descending data can assist in verification or three-dimensional deformation calculation [33–35].

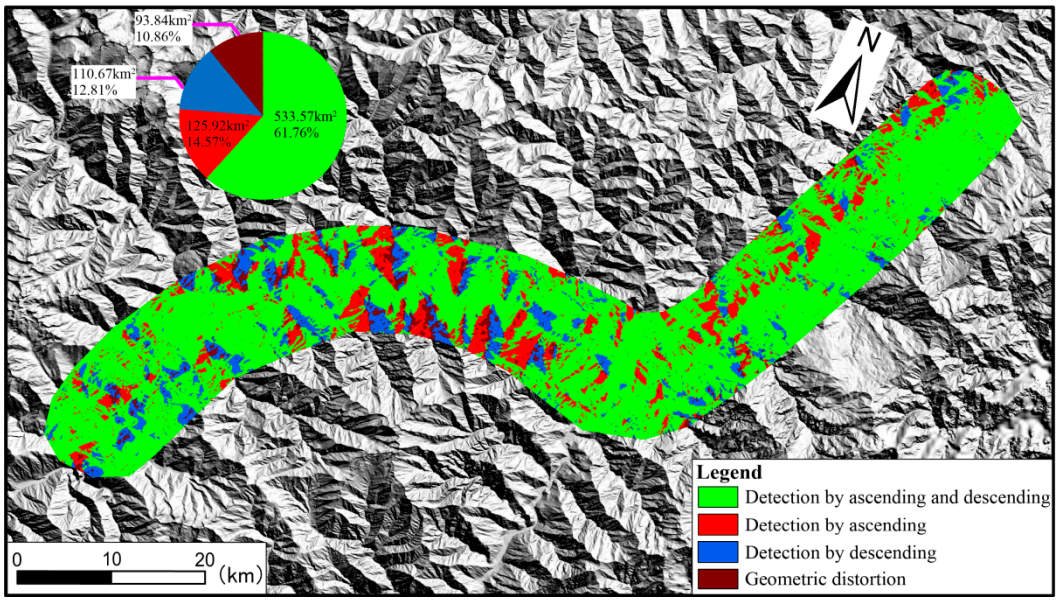

Figure 11. Geometrical distortions (layover and shadow) and visibility of the ascending and descending Sentinel−1 images in the study area.

5.2. Distribution Pattern of the Detected Landslides

There are many factors affecting landslide activities, including natural factors and human factors. However, since the study area is located in the valley along the National Highway (G317 and G213) from Mao County to Li County, InSAR deformation results are distributed about 5 km along both banks of the National Highway (G317 and G213), so the elevation, slope, aspect, and other natural factors have little impact on the development of the landslide [13]. In this paper, the factors affecting the development and distribution of landslides are analyzed from only two aspects: stratigraphic lithology and fault zone distribution.

According to the relationship between the distribution of active landslides and fault zones (Figure 12a), 33 of 115 active landslides in the study area intersected with fault zones, which were A15, A16/D12, A18, A19/D11, A30, A33 and A34/D21, A44, A45, A46/D46, A47/D47, A51/D54, A52/D57, A56, A57, A58, A59, A60, A61, A63, D19, D26, D44, D45, D49, D50, D53, D56, D58, D60, D68, D70, and D75, respectively, while the remaining 82 active landslides had no fault zones around them. Through field investigation, it is found that the landslide rock mass near the fault zone is relatively broken (Figure 12b). Because a small magnitude of crustal movement near the fault zone occurs during the monitoring interval, the broken rock mass leads to poor structure of the strata near the fault zone. Under the influence of external factors such as rainfall, earthquake, and river, landslide deformation is easy to occur [36].

The relationship between the landslide and the strata indicates that the lithology of the strata in the study area is complex from the Mesozoic Triassic to the Mesoproterozoic (Figure 12a). The hardness of rock can be divided into very hard rock, hard rock, relatively hard rock, relatively soft rock, soft rock, and very soft rock. A total of 12 landslides were distributed in relatively soft rock strata, 3 landslides were distributed in soft rock strata, 7 landslides were distributed in extremely hard rock strata, 4 were landslides distributed in soft to extremely hard rock strata, 1 landslide was distributed in very soft to extremely soft rock strata, 4 landslides were distributed in the relatively soft to relatively hard rock

strata, and 2 landslides were distributed in relatively soft to extremely hard rock strata. In summary, the texture of the landslide strata is unevenly distributed, and the strength of shale, argillaceous limestone, sands, and mudstone is low. Moreover, earthquake hazards are frequent in this region, with 11 earthquakes occurring between 2019 to 2021 (Figure 7). Therefore, under the interaction of natural and human factors such as rainfall, earthquake, water level, and human engineering activities, landslide hazards are easy to occur [14,37,38].

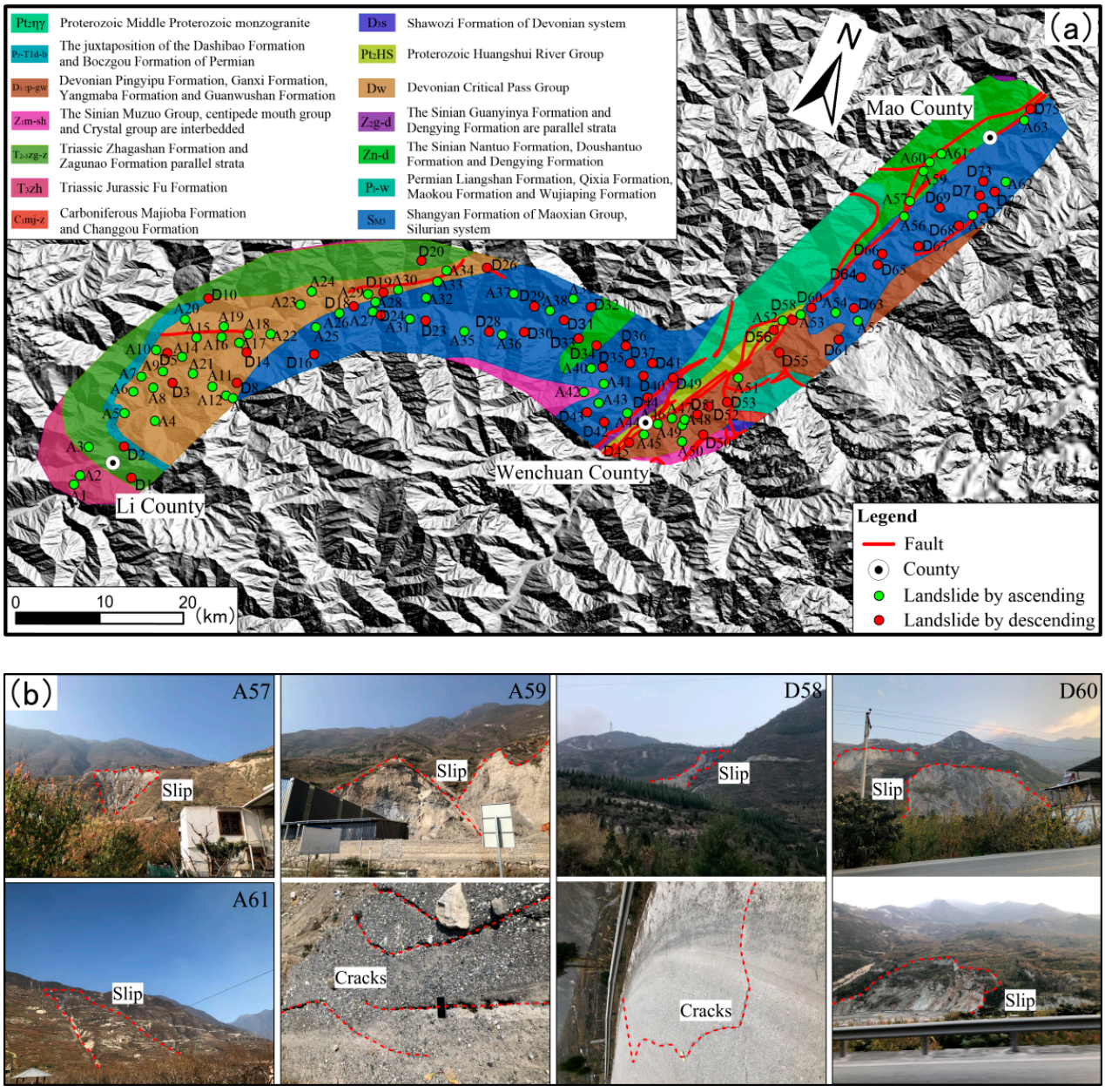

Figure 12. (**a**) Development and distribution of active landslides; (**b**) field verification pictures of A57, A59, A61, D58, and D60 slopes in (**a**).

According to the analysis of the fault zone and stratigraphic lithology in the study area, it can be concluded that the landslide hidden danger near the fault zone is controlled by the fault zone, the landslide rock mass across different strata is relatively broken, and the landslide hidden danger not controlled by the fault zone develops slowly. The combined effect of natural factors and human factors leads to the decrease of landslide stability.

5.3. Causative Factors of Landslide Activities

According to the deformation distribution characteristics, three landslides (A19, D44, D62) in Figures 5 and 6 are selected to explore the causes of landslide activities along the National Highway (G317 and G213) from Mao County to Li County. The first is the Qijiazhai landslide (A19), which is located in Rierjiao Village, Ganbao Township, Li County. The landslide has a transverse width of 2373 m and a longitudinal length of 1402 m. The second is the Longshan landslide (D44), which is located in Zengpo Village, Weizhou Town, Wenchuan County. The landslide has a transverse width of 2312 m and a longitudinal length of 2554 m. The third is the Sanchang Village landslide (D62), which is located in Sanchang Village, Nanxin Town, Mao County. The landslide has a transverse width of 1921 m and a longitudinal length of 3044 m. Google Earth optical remote sensing images showed that the foot of the three landslides intersected with the river (Figures 13a, 14a and 15a).

Figures 13a, 14a and 15a, respectively, show the annual average deformation rates of Qijiazhai landslide, Longshan landslide, and Sanchang landslide from January 2019 to December 2021, which are obtained by SBAS−InSAR technology based on the ascending and descending Sentinel−1 data. Figures 13b,c, 14b,c and 15b,c show the time series deformation of P1 and P2, P3 and P4, P5 and P6 (white circle marks in Figures 13a, 14a and 15a) with monthly rainfall, respectively. As shown in Figures 13a, 14a and 15a, strong deformation areas were detected in the front and middle parts of the Qijiazhai landslide, and the maximum deformation rate was about −45 mm/yr. Strong deformation areas were detected in the middle and back of Longshan landslide, and the maximum deformation rate was about −77 mm/yr. Strong deformation areas were detected in the middle and back of Sanchang landslide, and the maximum deformation rate was about −42 mm/yr. As shown in Figures 13b,c, 14b,c and 15b,c, the deformation generated by landslide is closely related to rainfall, and the increase of rainfall leads to the intensification of landslide deformation. Li County and Wenchuan County have abundant rainfall, while Mao County lacks rainfall. The deformation of Qijiazhai landslide was slow before April 2019, and the continuous heavy rainfall caused the landslide to be reactivated and the deformation to be accelerated. From November 2019 to April 2020, the deformation slowed down due to the decrease in precipitation. When a heavy rainfall of more than 200 mm occurred in June 2020, the deformation accelerated. Between November 2020 and May 2021, the deformation decreased due to the decrease in precipitation. However, when a heavy rainfall of more than 80 mm occurred again in May 2021, the deformation accelerated significantly. Due to abundant rainfall in Wenchuan County and monthly rainfall throughout the year, the Longshan landslide was in a linear deformation state from January 2019 to May 2020 and from October 2020 to May 2021. However, due to the increase in precipitation from June 2020 to September 2020 and May 2021 to September 2021, the deformation was significantly accelerated. However, it still does not affect the overall stable downward trend. The Sanchang village landslide was in a stable state before June 2019, but due to rainfall, the landslide was reactivated, and the deformation accelerated. From September 2019 to February 2020, the deformation decreased due to the decrease in precipitation. When a heavy rainfall of more than 90 mm occurred in May 2020, the deformation accelerated. Between November 2020 and April 2021, the deformation decreased due to the decrease in precipitation. However, when a heavy rainfall of more than 90 mm occurred again in May 2021, the deformation accelerated significantly. Based on the above analysis, it is shown that rainfall is an important factor affecting landslide activities along the National Highway (G317 and G213) from Mao County to Li County.

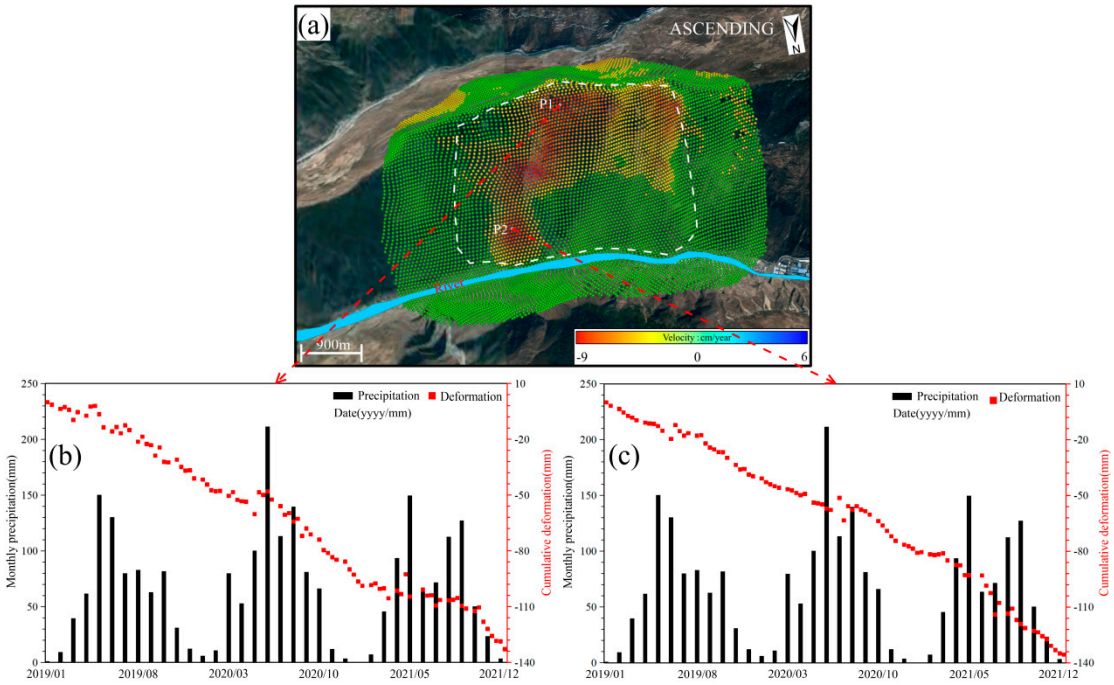

Figure 13. Relationship between slope deformation and precipitation for the Qijiazhai landslide with ascending data. (**a**) Annual deformation rate from 9 January 2019 to 24 December 2021; (**b**) time series deformation of Point P1 against monthly precipitation; and (**c**) time series deformation of Point P2 against monthly precipitation.

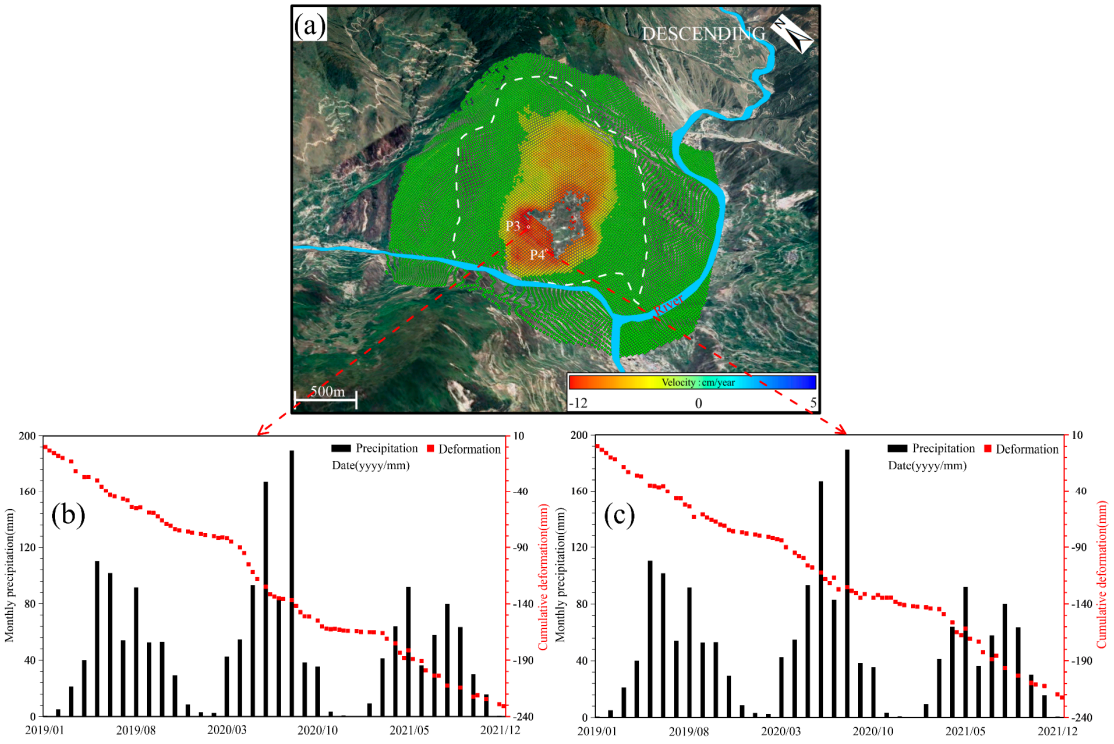

Figure 14. Relationship between slope deformation and precipitation for the Longshan landslide with descending data. (**a**) Annual deformation rate from 4 January 2019 to 13 December 2021; (**b**) time series deformation of Point P3 against monthly precipitation; and (**c**) time series deformation of Point P4 against monthly precipitation.

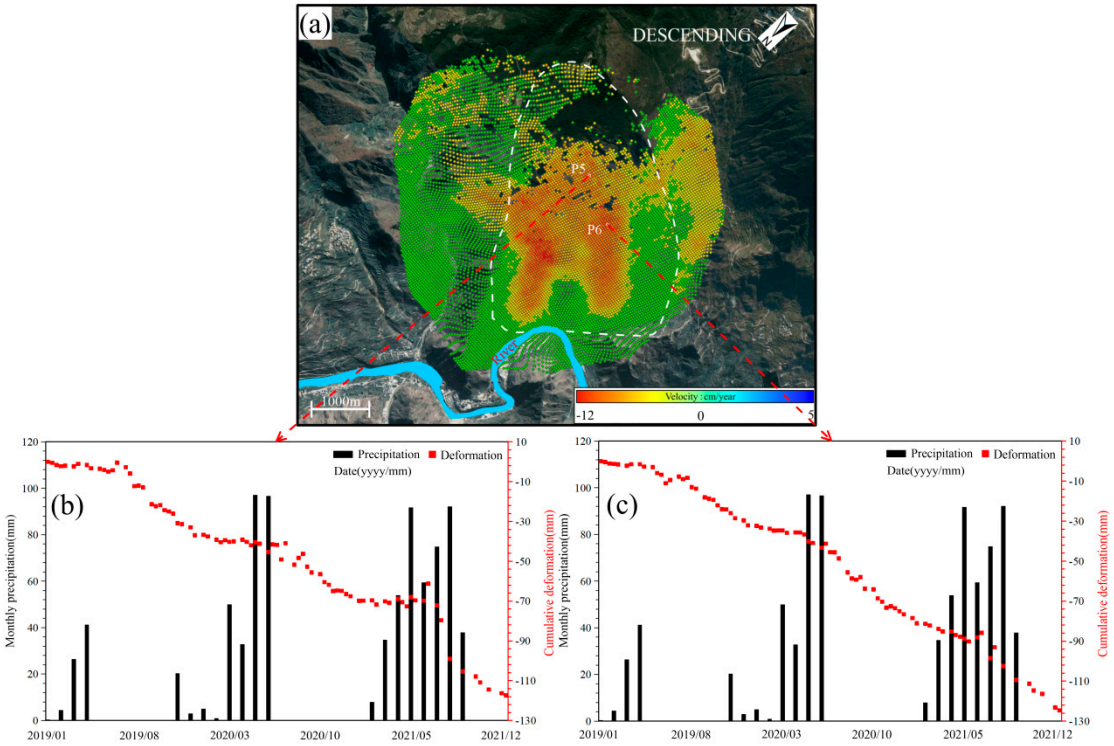

Figure 15. Relationship between slope deformation and precipitation for the Sanchang village landslide with ascending data. (**a**) Annual deformation rate from 4 January 2019 to 13 December 2021; (**b**) time series deformation of Point P5 against monthly precipitation; and (**c**) time series deformation of Point P6 against monthly precipitation.

6. Conclusions

In this paper, the quantitative suitability analysis of ascending and descending Sentinel−1 data is conducted. The results show that the combination of different orbit data along the National Highway (G317 and G213) from Mao County to Li County with complex topography can compensate the missing detection problem caused by a single imaging geometry, and thus avoid the acquisition of wrong deformation information in realizing the comprehensive and accurate early identification of landslide hazards.

According to the joint interpretation of deformation information obtained by SBAS−InSAR technology and optical remote sensing interpret, 115 active landslides were identified. Among them, 63 and 75 active landslides were identified using ascending and descending Sentinel−1 data. There were 12 more active landslides identified by descending data than ascending, and 23 active landslides were identified by ascending and descending data together. Through field investigation, it is found that almost all the 33 landslides intersecting with the fault zone are controlled by the fault, the landslide rock mass near the fault is relatively broken, and the strata developed by the active landslide may not be controlled by the fault. The time series analysis of deformation shows that the deformation rate of landslide is positively correlated with rainfall. Under the joint action of natural factors and human factors, the active landslide hidden danger is widely distributed in the study area. Therefore, it is very important to carry out high-frequency monitoring of landslides along the National Highway (G317 and G213) from Mao County to Li County, and even in the mountainous areas of southwest China, as well as prevention and early warning of geohazards.

Through this study, the effectiveness and advantage of SBAS−InSAR technology in the early identification of the hidden danger of mountain gorge landslides are revealed, which provides an important reference for landslide identification and analysis under complex terrain in China and even the world.

Author Contributions: P.R.: responsible for data processing, analysis, and writing the first draft of the paper; S.L.: leading the experimental design, providing technical guidance, and repeatedly and carefully revising the paper; G.Z., X.W. and M.M.: participated in data analysis and chart drawing; L.L., Y.C., H.H., Y.Y. and X.L.: providing basic data and revision verification. All authors have read and agreed to the published version of the manuscript.

Funding: This study was funded by the 1:50,000 Regional Geological Survey Project of H46E020004, H46E020005, and H46E020006 in the Rongbu area, Tibet (12120101000150014-47, DD20160015-06).

Institutional Review Board Statement: Not applicable.

Informed Consent Statement: Not applicable.

Data Availability Statement: All radar data are available through ESA.

Acknowledgments: We are very grateful to the European Space Agency (ESA) for providing free Sentinel−1 data, the Japan Aerospace Exploration Agency (JAXA) for providing free 30 m resolution "ALOS World 3D-30m" DEM, and the China earthquake networks center for providing free historical earthquake records along the National Highway (G317 and G213) from Mao County to Li County.

Conflicts of Interest: The authors declare no conflict of interest.

References

1. Cui, P.; Zhu, Y.Y.; Han, Y.S.; Chen, X.Q.; Zhuang, J.Q. The 12 May Wenchuan earthquake-induced landslide lakes: Distribution and preliminary risk evaluation. *Landslides* **2009**, *6*, 209–223. [CrossRef]
2. Chigira, M.; Wu, X.; Inokuchi, T.; Wang, G. Landslides induced by the 2008 Wenchuan earthquake, Sichuan, China. *Geomorphology* **2010**, *118*, 225–238. [CrossRef]
3. Yin, Y.; Wang, F.; Sun, P. Landslide hazards triggered by the 2008 Wenchuan earthquake, Sichuan, China. *Landslides* **2009**, *6*, 139–152. [CrossRef]
4. Meng, W.; Xu, Y.; Cheng, W.C.; Arulrajah, A. Landslide event on 24 June in Sichuan Province, China: Preliminary investigation and analysis. *Geosciences* **2018**, *8*, 39. [CrossRef]
5. Li, W.; Xu, Q.; Lu, H.; Dong, X.; Zhu, Y. Tracking the deformation history of large-scale rocky landslides and its enlightenment. *Geomat. Inf. Sci. Wuhan Univ.* **2019**, *44*, 1043–1053.
6. Dai, K.; Liu, G.; Li, Z.; Li, T.; Yu, B.; Wang, X.; Singleton, A. Extracting vertical displacement rates in Shanghai (China) with multi-platform SAR images. *Remote Sens.* **2015**, *7*, 9542–9562. [CrossRef]
7. Hu, L.; Dai, K.; Xing, C.; Li, Z.; Tomás, R.; Clark, B.; Shi, X.; Chen, M.; Zhang, R.; Qiu, Q.; et al. Land subsidence in Beijing and its relationship with geological faults revealed by Sentinel−1 InSAR observations. *Int. J. Appl. Earth Obs. Geoinf.* **2019**, *82*, 101886. [CrossRef]
8. Dai, K.; Ran, P.; Li, Z.; Austin, J.; Muller, J.P.; Zeng, Q.; Zhang, J.; Hu, L. Land Subsidence in Xiong'an New Area, China Revealed by InSAR Observations. *J. Geod. Geoinf. Sci.* **2021**, *4*, 70.
9. Zhuo, G.; Dai, K.; Huang, H.; Li, S.; Shi, X.; Feng, Y.; Li, T.; Dong, X.; Deng, J. Evaluating potential ground subsidence geo-hazard of Xiamen Xiang'an new airport on reclaimed land by SAR interferometry. *Sustainability* **2020**, *12*, 6991. [CrossRef]
10. Casu, F.; Elefante, S.; Imperatore, P.; Zinno, I.; Manunta, M.; De Luca, C.; Lanari, R. SBAS-DInSAR parallel processing for deformation time-series computation. *IEEE J. Sel. Top. Appl. Earth Obs. Remote Sens.* **2014**, *7*, 3285–3296. [CrossRef]
11. Ardizzone, F.; Bonano, M.; Giocoli, A.; Lanari, R.; Marsella, M.; Pepe, A.; Perrone, A.; Piscitelli, S.; Scifoni, S.; Scutti, M.; et al. Analysis of ground deformation using SBAS-DInSAR technique applied to COSMO-SkyMed images, the test case of Roma urban area. In *SAR Image Analysis, Modeling, and Techniques XII*; SPIE: Bellingham, WA, USA, 2012; Volume 8536, pp. 65–75.
12. Dai, C.; Li, W.; Wang, D.; Lu, H.; Xu, Q.; Jian, J. Active landslide detection based on Sentinel−1 data and InSAR technology in Zhouqu county, Gansu province, Northwest China. *J. Earth Sci.* **2021**, *32*, 1092–1103. [CrossRef]
13. Dun, J.; Feng, W.; Yi, X.; Zhang, G.; Wu, M. Detection and mapping of active landslides before impoundment in the baihetan reservoir area (China) based on the time-series InSAR method. *Remote Sens.* **2021**, *13*, 3213. [CrossRef]
14. Liu, X.; Zhao, C.; Zhang, Q.; Lu, Z.; Li, Z.; Yang, C.; Zhu, W.; Liu-Zeng, J.; Chen, L.; Liu, C. Integration of Sentinel−1 and ALOS/PALSAR-2 SAR datasets for mapping active landslides along the Jinsha River corridor, China. *Eng. Geol.* **2021**, *284*, 106033. [CrossRef]
15. Kropatsch, W.G.; Strobl, D. The generation of SAR layover and shadow maps from digital elevation models. *IEEE Trans. Geosci. Remote Sens.* **1990**, *28*, 98–107. [CrossRef]
16. Colesanti, C.; Wasowski, J. Investigating landslides with space-borne Synthetic Aperture Radar (SAR) interferometry. *Eng. Geol.* **2006**, *88*, 173–199. [CrossRef]
17. Cigna, F.; Bateson, L.B.; Jordan, C.J.; Dashwood, C. Simulating SAR geometric distortions and predicting Persistent Scatterer densities for ERS-1/2 and ENVISAT C-band SAR and InSAR applications: Nationwide feasibility assessment to monitor the landmass of Great Britain with SAR imagery. *Remote Sens. Environ.* **2014**, *152*, 441–466. [CrossRef]

18. Zhao, S.; Chigira, M.; Wu, X. Gigantic rockslides induced by fluvial incision in the Diexi area along the eastern margin of the Tibetan Plateau. *Geomorphology* **2019**, *338*, 27–42. [CrossRef]
19. Dong, J.; Zhang, L.; Li, M.; Yu, Y.; Liao, M.; Gong, J.; Luo, H. Measuring precursory movements of the recent Xinmo landslide in Mao County, China with Sentinel−1 and ALOS-2 PALSAR-2 datasets. *Landslides* **2018**, *15*, 135–144. [CrossRef]
20. Dai, K.; Li, Z.; Tomás, R.; Liu, G.; Yu, B.; Wang, X.; Cheng, H.; Chen, J.; Stockamp, J. Monitoring activity at the Daguangbao mega-landslide (China) using Sentinel−1 TOPS time series interferometry. *Remote Sens. Environ.* **2016**, *186*, 501–513. [CrossRef]
21. Hu, Q. Study Evaluation of Engineering Effect of Geological Disaster Prevention and Control in Western Sichuan. Ph.D. Thesis, Chengdu University of Technology, Chengdu, China, 2020.
22. Fang, Q. An Calculation Method for Predicting Runout Volume of Break Debris Flow in the Wenchuan Earthquake Area. Master's Thesis, Chengdu University of Technology, Chengdu, China, 2016.
23. Qu, T.; Lu, P.; Liu, C.; Wu, H.; Shao, X.; Wan, H.; Li, N.; Li, R. Hybrid-SAR technique: Joint analysis using phase-based and amplitude-based methods for the Xishancun giant landslide monitoring. *Remote Sens.* **2016**, *8*, 874. [CrossRef]
24. Dai, K.; Xu, Q.; Li, Z.; Tomás, R.; Fan, X.; Dong, X.; Li, W.; Zhou, Z.; Gou, J.; Ran, P. Post-disaster assessment of 2017 catastrophic Xinmo landslide (China) by spaceborne SAR interferometry. *Landslides* **2019**, *16*, 1189–1199. [CrossRef]
25. Berardino, P.; Fornaro, G.; Lanari, R.; Sansosti, E. A new algorithm for surface deformation monitoring based on small baseline differential SAR interferograms. *IEEE Trans. Geosci. Remote Sens.* **2002**, *40*, 2375–2383. [CrossRef]
26. Guo, J.; Hu, J.; Li, B.; Zhou, L. Land subsidence in Tianjin for 2015 to 2016 revealed by the analysis of Sentinel−1A with SBAS−InSAR. *J. Appl. Remote Sens.* **2017**, *11*, 026024. [CrossRef]
27. Lanari, R.; Mora, O.; Manunta, M.; Berardino, P.; Sansosti, E. A small-baseline approach for investigating deformations on full-resolution differential SAR interferograms. *IEEE Trans. Geosci. Remote Sens.* **2004**, *42*, 1377–1386. [CrossRef]
28. Lanari, R.; Casu, F.; Manzo, M.; Zeni, G.; Berardino, P.; Manunta, M.; Pepe, A. An overview of the small Baseline subset algorithm: A DInSAR technique for surface deformation analysis. *Pure Appl. Geophys.* **2007**, *164*, 637–661. [CrossRef]
29. Goldstein, R. Atmospheric limitations to repeat-track radar interferometry. *Geophys. Res. Lett.* **1995**, *22*, 2517–2520. [CrossRef]
30. Gou, J. Early Identification of Landslides Based on InSAR with Elevation Related Atmospheric Correction. Master's Thesis, Chengdu University of Technology, Chengdu, China, 2020.
31. Zhang, L.; Dai, K.; Deng, J.; Ge, D.; Liang, R.; Li, W.; Xu, Q. Identifying potential landslides by stacking-InSAR in southwestern China and its performance comparison with SBAS−InSAR. *Remote Sens.* **2021**, *13*, 3662. [CrossRef]
32. Wasowski, J.; Bovenga, F. Investigating landslides and unstable slopes with satellite Multi Temporal Interferometry: Current issues and future perspectives. *Eng. Geol.* **2014**, *174*, 103–138. [CrossRef]
33. Shi, X.; Zhang, L.; Liao, M.; Balz, T. Deformation Monitoring of Slow-moving Landslide with L-and C-Band SAR Interferometry. *Remote Sens. Lett.* **2014**, *5*, 951–960. [CrossRef]
34. Liu, G.; Zhang, R.; Li, T.; Yu, B.; Li, T.; Jia, H.; Nie, Y. Extraction of 3D Surface Deformation Velocity Field Based on Multi-satellite Platform Permanent Scatterer Radar Interference. *J. Geophys.* **2012**, *55*, 2598–2610.
35. Hu, J.; Li, Z.; Ding, X.; Zhu, J.; Zhang, L.; Sun, Q. Resolving Three-Dimensional Surface Displacements from InSAR Measurements: A Review. *Earth-Sci. Rev.* **2014**, *133*, 1–17. [CrossRef]
36. Zuo, X.F. Study on the Influence of Active Fault on Slope Hazards in Ningqiang County. Master's Thesis, Xi'an University of Science and Technology, Xi'an, China, 21 July 2020.
37. Liang, R.; Dai, K.; Shi, X.; Guo, B.; Dong, X.; Liang, F.; Tomás, R.; Wen, N.; Fan, X. Automated mapping of ms 7.0 jiuzhaigou earthquake (China) post-disaster landslides based on high-resolution UAV imagery. *Remote Sens.* **2021**, *13*, 1330. [CrossRef]
38. Shi, X.; Yang, C.; Zhang, L.; Jiang, H.; Liao, M.; Zhang, L.; Liu, X. Mapping and characterizing displacements of active loess slopes along the upstream Yellow River with multi-temporal InSAR datasets. *Sci. Total Environ.* **2019**, *674*, 200–210. [CrossRef] [PubMed]